5-1-2020

Orbital Refinement and Stellar Properties for the HD 9446, HD 43691, and HD 179079 Planetary Systems

Michelle L. Hill
University of California, Riverside

Teo Močnik
University of California, Riverside

Stephen R. Kane
University of California, Riverside

Gregory W. Henry
Tennessee State University

Joshua Pepper
Lehigh University

See next page for additional authors

Recommended Citation

Hill, M., Močnik, T., Kane, S., Henry, G., Pepper, J., Hinkel, N., Dalba, P., Fulton, B., Stassun, K., Rosenthal, L., Howard, A., Howell, S., Everett, M., Boyajian, T., Fischer, D., Rodriguez, J., Beatty, T., & James, D. (2020). Orbital Refinement and Stellar Properties for the HD 9446, HD 43691, and HD 179079 Planetary Systems. *Astronomical Journal, 159* (5) https://doi.org/10.3847/1538-3881/ab7d33

The Astronomical Journal, 159:197 (17pp), 2020 May https://doi.org/10.3847/1538-3881/ab7d33

Orbital Refinement and Stellar Properties for the HD 9446, HD 43691, and HD 179079 Planetary Systems

Michelle L. Hill[1], Teo Močnik[1], Stephen R. Kane[1], Gregory W. Henry[2], Joshua Pepper[3], Natalie R. Hinkel[4], Paul A. Dalba[1,14], Benjamin J. Fulton[5], Keivan G. Stassun[6], Lee J. Rosenthal[5], Andrew W. Howard[5], Steve B. Howell[7], Mark E. Everett[8], Tabetha S. Boyajian[9], Debra A. Fischer[10], Joseph E. Rodriguez[11], Thomas G. Beatty[11], and David J. James[12,13]

[1] Department of Earth and Planetary Sciences, University of California, Riverside, CA 92521, USA; michelle.hill@email.ucr.edu
[2] Center of Excellence in Information Systems, Tennessee State University, Nashville, TN 37209, USA
[3] Department of Physics, Lehigh University, Bethlehem, PA 18015, USA
[4] Southwest Research Institute, San Antonio, TX 78238, USA
[5] Department of Astronomy, California Institute of Technology, Pasadena, CA 91125, USA
[6] Vanderbilt University, Department of Physics & Astronomy, 6301 Stevenson Center Lane, Nashville, TN 37235, USA
[7] NASA Ames Research Center, Moffett Field, CA 94035, USA
[8] National Optical Astronomy Observatory, Tucson, AZ 85719, USA
[9] Department of Physics and Astronomy, Louisiana State University, Baton Rouge, LA 70803, USA
[10] Department of Astronomy, Yale University, New Haven, CT 06511, USA
[11] Department of Astronomy and Steward Observatory, University of Arizona, Tucson, AZ 85721, USA
[12] Center for Astrophysics, Harvard & Smithsonian, 60 Garden Street, Cambridge, MA 02138, USA
[13] Black Hole Initiative at Harvard University, 20 Garden Street, Cambridge, MA 02138, USA
Received 2019 May 28; revised 2020 March 4; accepted 2020 March 4; published 2020 April 9

Abstract

The Transit Ephemeris Refinement and Monitoring Survey is a project that aims to detect transits of intermediate-long period planets by refining orbital parameters of the known radial velocity planets using additional data from ground-based telescopes, calculating a revised transit ephemeris for the planet, then monitoring the planet host star during the predicted transit window. Here we present the results from three systems that had high probabilities of transiting planets: HD 9446 b and c, HD 43691 b, and HD 179079 b. We provide new radial velocity (RV) measurements that are then used to improve the orbital solution for the known planets. We search the RV data for indications of additional planets in orbit and find that HD 9446 shows a strong linear trend of 4.8σ. Using the newly refined planet orbital solutions, which include a new best-fit solution for the orbital period of HD 9446 c, and an improved transit ephemerides, we found no evidence of transiting planets in the photometry for each system. Transits of HD 9446 b can be ruled out completely and transits HD 9446 c and HD 43691 b can be ruled out for impact parameters up to $b = 0.5778$ and $b = 0.898$, respectively, due to gaps in the photometry. A transit of HD 179079 b cannot be ruled out, however, due to the relatively small size of this planet compared to the large star and thus low signal to noise. We determine properties of the three host stars through spectroscopic analysis and find through photometric analysis that HD 9446 exhibits periodic variability.

Unified Astronomy Thesaurus concepts: Radial velocity (1332); Transit photometry (1709); Photometry (1234); Stellar photometry (1620); Ephemerides (464); Exoplanets (498); Exoplanet dynamics (490); Spectral energy distribution (2129); Proper motions (1295)

1. Introduction

Transiting exoplanets have become an integral part of exoplanetary science and provide not only detection and confirmation of exoplanets but also information about the radius and the atmospheric composition of the planet. Provided the star's size is known, the radius of the planet can be determined by the reduction in a star's flux as the planet passes in front of the star since the transit "depth" (or corrected depth if a close companion provides "third light" contamination) is directly proportional to the cross-sectional size of the planet. The atmospheric composition of the planet can be detected by the light from the star passing through the planet's atmosphere, through a method called transmission spectroscopy (Seager & Sasselov 2000).

Combined with the information gathered through the radial velocity (RV) method, transits enable studies of the mean density of a planet as well as its interior structure. Planets with both RV and transit observations are the most fully constrained and are the main data sources behind many statistical relationships that define our understanding of the formation and evolution of exoplanets, such as the mass–radius relationship and models of the composition of exoplanets. Thus detecting the potential transits of known RV planets is of great importance.

The Transit Ephemeris Refinement and Monitoring Survey (TERMS) is a project that seeks to detect transits of known RV planets with a broad range of orbital periods (Kane et al. 2009). The transit detection method is biased toward planets with short orbital periods close to their star as the probability of a planet transiting its star increases with decreasing distance from the star (Beatty & Gaudi 2008; Kipping & Sandford 2016). In order to detect planets further away from their star and broaden the catalog of transiting exoplanets, the TERMS team targets known intermediate- to long-period exoplanets with existing RV data in the literature. The orbital parameters of the known planets are first recalculated using the latest data from the Keck

[14] NSF Astronomy and Astrophysics Postdoctoral Fellow.

Table 1
Stellar Properties

Parameter	HD 9446 b[a]	HD 9446 c[a]	HD 43691 b[b]	HD 179079 b[b]
Star				
Spectral Type	G5 V	G5 V	G0	G5IV
V	8.35	8.35	8.03	7.95
Distance (pc)[c]	50.42 ± 0.35	50.42 ± 0.35	85.81 ± 0.37	69.848 ± 0.395
$T_{\rm eff}$ (K)[d]	5793 ± 22	5793 ± 22	6093	5646
$\log g$[d]	4.53 ± 0.16	4.53 ± 0.16	4.31 ± 0.07	4.11 ± 0.04
$F_{\rm bol}$ (10^{-8} erg s^{-1} cm^{-2})[d]	1.245 ± 0.029	1.245 ± 0.029	1.764 ± 0.020	2.084 ± 0.049
[Fe/H] (dex)[e]	0.13 ± 0.06	0.13 ± 0.06	0.32 ± 0.03	0.35 ± 0.09
M_* ($M_\odot$)[f]	1.07 ± 0.08	1.07 ± 0.08	1.32 ± 0.09	1.25 ± 0.09
R_* ($R_\odot$)[f]	0.984 ± 0.01	0.984 ± 0.01	1.704 ± 0.023	1.792 ± 0.016
ρ_* (g cm^{-3})[f]	1.59 ± 0.12	1.59 ± 0.12	0.375 ± 0.031	0.307 ± 0.023
Planet				
P (days)	30.052 ± 0.027	192.9 ± 0.9	36.9987 ± 0.0011	14.479 ± 0.010
e	0.2 ± 0.06	0.06 ± 0.06	0.0796 ± 0.0067	0.0490 ± 0.0870
ω (°)	215 ± 30	100 ± 130	292.7 ± 4.8	308 ± 77
K (m s^{-1})	46.6 ± 3.0	63.9 ± 4.3	130.06 ± 0.84	6.22 ± 0.78
$M_p \sin i$ (M_J)	0.7 ± 0.06	1.82 ± 0.17	2.55 ± 0.34	0.081 ± 0.02
a (au)	0.189 ± 0.006	0.654 ± 0.022	0.238 ± 0.015	0.1214 ± 0.0068

Notes.
[a] Planet parameters from Hébrard et al. (2010).
[b] Planet parameters from Ment et al. (2018).
[c] Gaia Collaboration et al. (2018).
[d] SWEETcat catalog Santos et al. (2013).
[e] Hypatia Catalog Hinkel et al. (2014).
[f] Our SED analysis.

Observatory. Then a refined transit ephemeris is determined for the planet so that the planet host star can be observed during the predicted transit window. Photometry from various ground-based telescopes including two of Tennessee State University's automated photoelectric telescopes (APTs) and the Kilodegree Extremely Little Telescope (KELT) are then analyzed to determine if a transit was detected.

In this paper we present an analysis of both the host star and the planets in the HD 9446, HD 43691, and HD 179079 systems. We provide new RV data for each system, extending the time baseline of the observations and so improving the orbital parameters of the planets. From this new data, we calculated an accurate transit ephemeris and predicted the parameters of a potential transit of each known planet. We present precision photometry of HD 9446, HD 43691, and HD 179079 acquired with the APTs and KELT and determine the existence of transits of each of the known planets in these systems. We note that each of these stars falls within the gaps of the primary mission for TESS and so are unlikely to be observed by space-based instruments in the near future.

2. Science Motivation

Each of the systems in this paper was detected by the RV method. The multiplanet system HD 9446 was first discovered by Hébrard et al. (2010) using the SOPHIE spectrograph. The initial orbital solution gave the inner planet (b) a period of 30.052 ± 0.027 days and the outer planet (c) a period of 192.9 ± 0.9 days. HD 43691 b was first discovered by da Silva et al. (2007), with orbital parameters updated in 2018 by Ment et al. (2018) including a refined orbital period for planet b of 36.9987 ± 0.0011 days. HD 179079 b was first discovered by Valenti et al. (2009), with updated orbital parameters including a period of 14.479 ± 0.010 days by Ment et al. (2018; see Table 1). As the precision of planetary and orbital parameters is inherently linked to how well the host star is known we present a spectral energy distribution (SED) analysis of each star in Section 3. Each of these systems has a planet that occupies the period space between 10 and 50 days and has relatively high transit probabilities (see Section 4) so were flagged as high-priority TERMS targets. Shown in Figure 1 are two diagrams that include the known transiting planets as small circles, where the data were extracted from the NASA Exoplanet Archive (Akeson et al. 2013) on 2019 December 1. Highlighted as orange circles are those transiting planets discovered using the RV method, such as HD 209458b (Charbonneau et al. 2000; Henry et al. 2000). The four planets in the three systems included in this study are indicated as large crosses. Note that these four planets are not known to transit, and so we use the radii estimates described in Section 4. The mass–radius diagram shown in the left panel indicates where the four planets fall with respect to the bulk of the known transiting planet population. HD 179079 b is expected to lie within the Neptune regime and could potentially be an interesting test of photo-evaporation for low-mass giant planets (Laughlin et al. 2011; Lopez & Fortney 2013). The remaining three planets fall within the bulk of the known transiting giant planets. However, the period–mass diagram shown in the right panel demonstrates that the three largest planets in our sample are significantly removed from the bulk of the known transiting giant planet population when considering orbital period. The detection of transits for such planets would therefore be of high value in studies of mass–radius relationships for "cold" giant planets, particularly since the host stars for the three systems of our sample are all exceptionally bright (see Section 3).

In order to detect the possible transit of the planetary systems, additional RV measurements were taken using the HIRES instrument on the Keck I telescope. Combining the

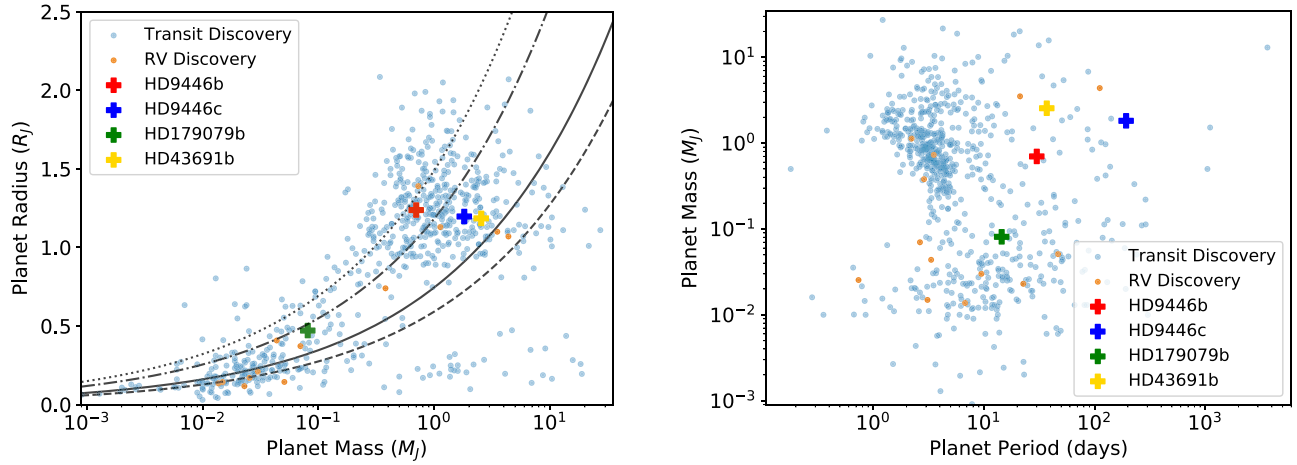

Figure 1. Location of the studied planets with respect to the known demographics of exoplanets. Left: mass–radius diagram of known transiting planets (small circles), including lines of constant density. The four planets included in this study are shown as large crosses, where the radii are estimated using the Chen & Kipping (2016) methodology (see Section 4). Right: period–mass diagram using the same planets as for the mass–radius diagram where the planets in our sample are similarly indicated as crosses.

newly obtained data with that already available for each system, the RV data was fit using the RV fitting tool RadVel (Fulton et al. 2018) to confirm each planet's orbital solution and look for linear trends (Section 5). These trends could potentially be indications of additional unidentified planets in the system. We search for unknown planets in the RV data and provide an analysis of the sensitivity of our search through RV injection-recovery tests in Section 5.3.

Using the transit window determined through RadVel along with the photometry from the KELT and the APTs, the newly calculated transit windows were then used to look for transits of each planet. These results are presented in Section 6.3.

The KELT and APT photometry were then used to characterize the stellar variability of each system. Starspots are a common cause of intrinsic stellar variability by inducing rotational modulation as the star rotates (e.g., Kipping 2012 and citations therein). The rotational modulation period is therefore a direct measurement of the rotational period of the star. When coupled with the spectroscopic measurement of the projected rotational velocity, it can be used to constrain the inclination of the stellar rotational axis, i_*.

3. Stellar Properties

As an independent determination of the basic stellar parameters, we performed an analysis of the broadband SED of each star together with the Gaia DR2 parallaxes (adjusted by +0.08 mas to account for the systematic offset reported by Stassun & Torres 2018), in order to determine an empirical measurement of the stellar radius, following the procedures described in Stassun & Torres (2016) and Stassun et al. (2017, 2018). We extracted the NUV flux from Galaxy Evolution Explorer, the B_TV_T magnitudes from Tycho-2, the Strömgren *ubvy* magnitudes from Paunzen (2015), the *BVgri* magnitudes from APASS, the JHK_S magnitudes from 2MASS, the W1–W4 magnitudes from WISE, and the G magnitude from Gaia, as available for each star. Together, the available photometry in general spans the full stellar SED over the wavelength range 0.2–22 μm (see Figure 2).

We performed a fit using Kurucz stellar atmosphere models (Kurucz 2013), with the effective temperature ($T_{\rm eff}$), metallicity ([Fe/H]), and surface gravity (log g) adopted from the systematic spectroscopic analyses provided in the SWEET catalog (Santos et al. 2013). The only free parameter is the extinction (A_V), which we restricted to the maximum line-of-sight value from the dust maps of Schlegel et al. (1998). The resulting fits are good (Figure 2) with a reduced χ^2 ranging from 1.9 to 3.4. Integrating the (unreddened) model SED gives the bolometric flux at Earth ($F_{\rm bol}$). Taking the $F_{\rm bol}$ and $T_{\rm eff}$ together with the Gaia DR2 parallax, gives the stellar radius. Finally, we can use the empirical relations of Torres et al. (2010) and a 6% error from the empirical relation itself to estimate the stellar mass; this, in turn, together with the stellar radius provides an empirical estimate of the mean stellar density. We used the derived radius and mass to calculate a value for log g and compared our values to those from the SWEET catalog (Santos et al. 2013). We found there is a good agreement (within the uncertainties) between the values for each star. The full set of resulting parameters is summarized in Table 1 along with planet properties of the three systems drawn from the Hébrard et al. (2010) and Ment et al. (2018) papers. Note that while HD 9446 and HD 43691 are similar to the Sun, HD 179079 is an evolved star that has entered the subgiant branch.

We observed the star HD 9446 using CHIRON, a fiber-fed Echelle spectrometer with a resolution of $R = 79{,}000$ (Tokovinin et al. 2013; Brewer et al. 2014) in use at the 1.5 m telescope at Cerro Tololo Inter-American Observatory (CTIO). The CHIRON spectrum was analyzed using Spectroscopy Made Easy (SME), described in detail by Valenti & Piskunov (1996) and Valenti & Fischer (2005). The stellar parameters derived for HD 9446 from our SME analysis are consistent with those shown in Table 1. The distances to the stars shown in Table 1 are from the Gaia Data Release 2 parallaxes (Gaia Collaboration et al. 2018).

The three host stars were found within the Hypatia Catalog,[15] an amalgamate database of stellar abundances for nearby FGKM-type stars (Hinkel et al. 2014). HD 9446 was observed by seven groups (Ramírez et al. 2007, 2009, 2012, 2013; Baumann et al. 2010; Brugamyer et al. 2011; Brewer et al. 2016), while HD 43691 and HD 179079 were both

[15] Data can be found on www.hypatiacatalog.com.

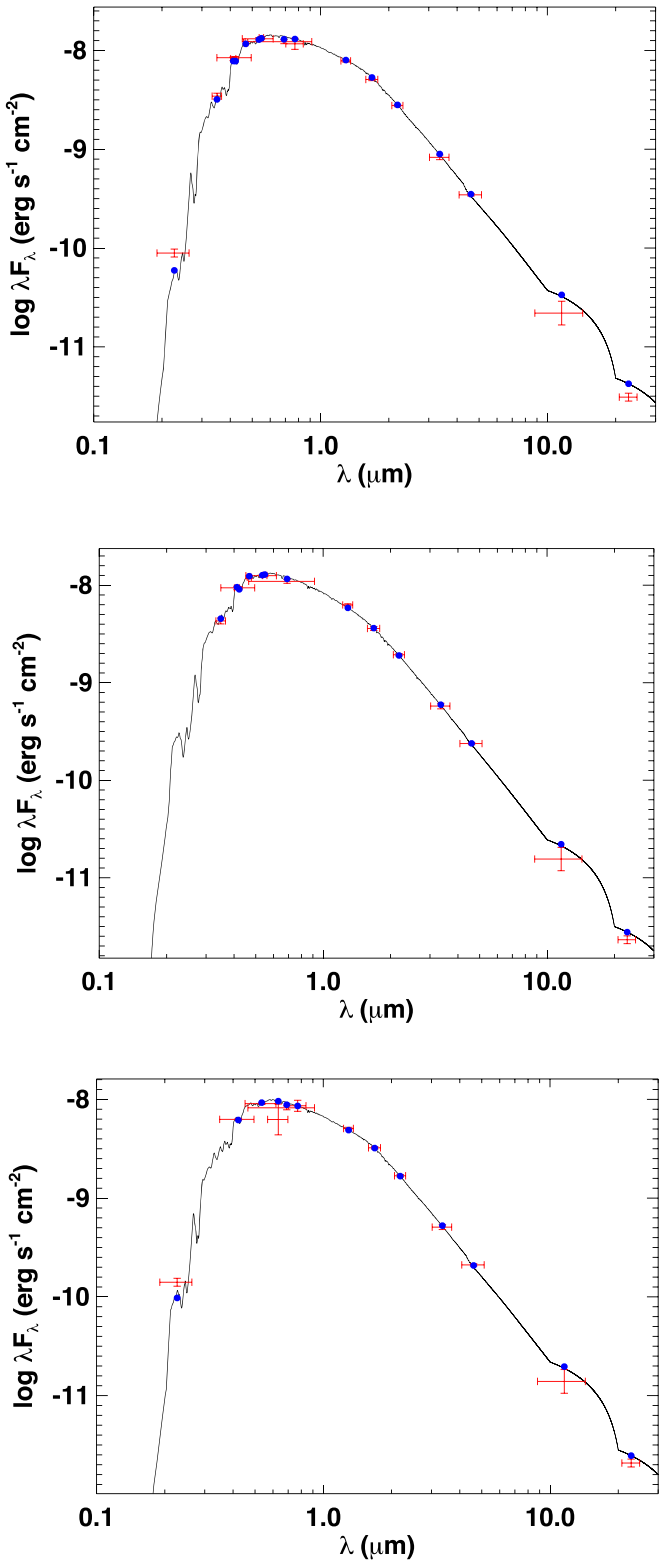

Figure 2. Spectral energy distributions (SEDs) of (a) HD 179079 with χ^2 value of 3.4, (b) HD 43691 χ^2 value of 1.9, and (c) HD 9446 χ^2 value of 2.0. Red symbols represent the observed photometric measurements, where the horizontal bars represent the effective width of the passband. Blue symbols are the model fluxes from the best-fit Kurucz atmosphere model (black).

observed by six groups (Gonzalez et al. 2010a, 2010b; Brugamyer et al. 2011; Kang et al. 2011; Petigura & Marcy 2011; Brewer et al. 2016 and Petigura & Marcy 2011; Maldonado et al. 2013; Ramírez et al. 2014; Jofré et al. 2015; Brewer et al. 2016; Maldonado & Villaver 2016, respectively). All data sets are renormalized to the same solar scale within Hypatia, namely Lodders et al. (2009), such that they are more easily comparable. Then, when multiple groups measure the same element within the same star, the median value is used and the uncertainty is defined as the spread or range from all of the renormalized abundance determinations. The [Fe/H] values for the three target stars are consistent with those in Table 1. The other elements, including volatiles, refractory, iron-peak, and neutron-capture, are all enriched to a similar magnitude as the respective [Fe/H] values when compared to the Sun. Of note, the composition of HD 9446 is the most similar to the Sun, such that a few elements (N, O, Na, Mg, Si, S, Mn, and Cu) hover around 0.0 dex when uncertainty is taken into account. All three stars are relatively close and bright, making the systems ideal for additional characterization.

We also examine the stars for possible evidence of binary companions. HD 9446 was previously observed using speckle imaging by Wittrock et al. (2016), for which the data found no evidence of a stellar companion. Here we provide new results for one of the stars, HD 179079, using data from the Differential Speckle Survey Instrument (DSSI). DSSI is a dual-channel speckle imaging system that uses two narrowband filters with wavelengths centered on 692 and 880 nm. The details of the instrument hardware and data reduction are described in detail by Horch et al. (2009) and Howell et al. (2011). HD 179079 was observed using DSSI as part of a survey of known exoplanet host stars for binary companions (Kane et al. 2014, 2019; Wittrock et al. 2016, 2017). The star was observed using WIYN on 2016 April 19 and Gemini-South on 2016 June 29 during which periods DSSI was mounted as a guest instrument at these telescopes. No companion was detected in any of the images from our observations, with a detection limit of $\Delta m \sim 7$ magnitudes in both channels within the range of $0\farcs1$–$1\farcs8$. Given the distance to the star listed in Table 1, this corresponds to a projected range of 7–125 au for which companions of most spectral types can be excluded based on our analysis.

4. Transit Probability

As TERMS targets, these planets had a relatively high likelihood of transiting their host star. Using the equation from Kane & von Braun (2008) the prior transit probability can be estimated by:

$$P_t = \frac{(R_p + R_*)[1 + e\cos(\pi/2 - \omega)]}{a(1 - e^2)}, \quad (1)$$

where R_* is the radius of the star, e is the orbital eccentricity, ω is the argument of periastron, a is the semimajor axis, and the planet radius (R_p) is determined using the mass–radius relation code Forecaster developed by Chen & Kipping (2016). Our calculation does not compute the posterior transit probability, which includes prior information for the mass distribution of RV-discovered exoplanets (Ho & Turner 2011; Stevens & Gaudi 2013). Simulations by Stevens & Gaudi (2013) found only a ∼1% difference between prior and posterior transit probabilities for planets with masses in the range 100–1000 $M_\oplus$, which likely includes HD 9446 b, HD 9446 c, and HD 43691 b. For HD 179079 b, the posterior transit probability is likely higher than the prior transit probability by ∼20% (Stevens & Gaudi 2013).

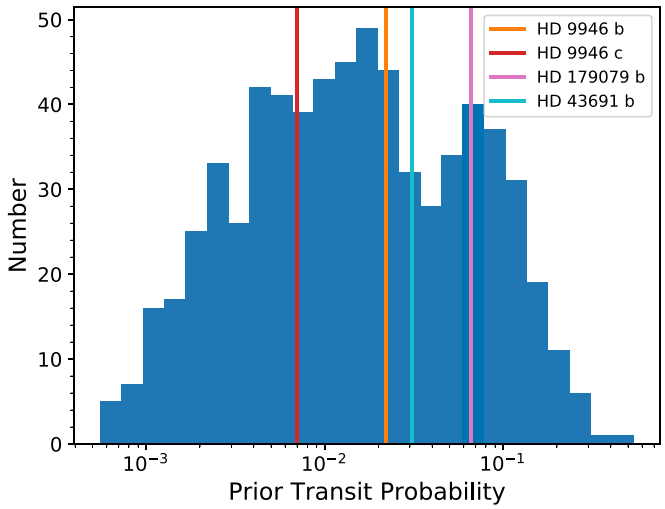

Figure 3. Prior transit probabilities for the four target planets compared to the distribution of prior transit probabilities for RV-discovered planets from Dalba et al. (2019).

Calculating the transit probability (Equation (1)) with the planet radii estimated by Forecaster (Chen & Kipping 2016) we find that HD 9446 b, with an estimated planet radius of $1.238 \pm 0.240\ R_J$, has a transit probability of ~2.2% with a transit depth of $1.671 \times 10^{-2} \pm 7.1 \times 10^{-3}$. For HD 9446 c, with a radius of $1.197 \pm 0.226\ R_J$, the transit probability is ~0.7% with an expected transit depth of $1.563 \times 10^{-2} \pm 6.4 \times 10^{-3}$. For HD 179079 b, with a calculated radius of $0.471 \pm 0.1935\ R_J$, the transit probability is ~6.6% with a depth of $7.29 \times 10^{-4} \pm 7.2 \times 10^{-4}$, and for HD 43691 b, with a calculated planet radius of $1.185 \pm 0.218\ R_J$, transit probability is ~3.1% with a depth of $5.107 \times 10^{-3} \pm 2.05 \times 10^{-3}$.

We consider the transit probabilities of the four target planets with those of the full sample of RV-discovered exoplanets. We acquire the prior transit probabilities for 673 RV-discovered exoplanets from Dalba et al. (2019), which we display in Figure 3. These probabilities do not account for the known mass distribution of the sample of RV exoplanets and, therefore, are not posterior transit probabilities (Ho & Turner 2011; Stevens & Gaudi 2013). The transit probabilities we calculated with Equation (1) for HD 9446 b and c, HD 43691 b, and HD 179079 b are also prior probabilities, meaning they can be compared with those from Dalba et al. (2019). All four of these transit probabilities fall within one standard deviation of the median of the distribution (Figure 3). However, all probabilities except that of HD 9446 c are higher than the median. This suggests that these targets were relatively good candidates for transit searches especially considering their orbital periods.

5. Radial Velocity Analysis

5.1. Data Acquisition: Spectroscopy

Spectroscopic data for each target was obtained by the high-resolution echelle spectrometer (HIRES) on the 10.0 m Keck I telescope. The details of the instrument hardware and data reduction are described in detail by Vogt et al. (1994). This data, along with that available from the ELODIE (Baranne et al. 1996) and SOPHIE spectrographs (Perruchot et al. 2008) was used to confirm the orbital solutions of the systems using RadVel (see Table 2 for observation details). The complete RV data set analyzed is available in Appendix A.

5.2. Orbital Solutions and Linear Trends

Here we present the revised orbital solutions for HD 9446, HD 43691, and HD 179079.

Each star's RV data was fit using the RV modeling toolkit RadVel (Fulton et al. 2018) in order to confirm the orbital solution and look for linear trends to determine if there were indications for additional planetary companions. RadVel enables users to model Keplerian orbits in RV time series. RadVel fits RVs using maximum a posteriori probability (MAP) and employs "modern Markov chain Monte Carlo (MCMC) sampling techniques and robust convergence criteria to ensure accurately estimated orbital parameters and their associated uncertainties" (Fulton et al. 2018). Once the MCMC chains are well mixed and the orbital parameters that maximize the posterior probability are found, RadVel then supplies an output of the final parameter values from the MAP fit, provides RV time series plots and MCMC corner plots showing all joint posterior distributions derived from the MCMC sampling.

RadVel also provides a mid transit time of each planet along with uncertainties, which when combined with the expected transit duration of the planet defines the estimated transit window of the planet.

A Keplerian orbital solution was fit to the RV data for HD 9446, HD 179079, and HD 43691 using RadVel in order to refine the orbital parameters and transit ephemeris of each system. Public RV data from SOPHIE and ELODIE published in da Silva et al. (2007) and Hébrard et al. (2010) was combined with our Keck HIRES data, which is provided in full in Tables A1, A2, and A3 in Appendix A. Gamma velocities of 21712.56 $m\,s^{-1}$, $-28967.79\ m\,s^{-1}$, and $-28958.18\ m\,s^{-1}$ were subtracted from the total RV values of the SOPHIE data for HD 9446, SOPHIE data for HD 43691 and ELODIE data for HD 43691, respectively, before being run through RadVel. Thus the gamma values in Tables 3–5 (σ) are in reference to these values. Tables 3–5 list the resulting median values of the posterior distributions for each parameter in the orbital solutions. The best-fit Keplerian orbital model for the system and planet orbital solutions are shown for the HD 9446 b and HD 9446 c planets in Figure 4, for planet HD 179079 b in Figure 5, and for planet HD 43691 b in Figure 6. Comparing these results with those from Table 1, each planet's orbital solution is in close agreement with the published values with the exception of HD 9446 c. Our fit presents a new best-fit period of this planet of 189.6 ± 0.13 days. Note all other variances for HD 9446 c fall within the uncertainties of the published values. We fit each system allowing the trend parameter to be free in order to look for linear trends. These trends could be indications of additional unknown planets in orbit around the host star. RadVel provides a model comparison summary with both Akaike information criterion (AIC) and Bayesian information criterion (BIC) values. The results from these model comparisons can be found in Tables B1, B2, and B3 in Appendix B. For HD 179079 both AIC and BIC methods preferred the model without a trend (see Table B3). For HD 43691 both the AIC and BIC preferred the model with a $\sim 1.75\sigma$ trend (see Tables 5 and B2). While this could indicate the presence of another unknown planet in the system, this is a low sigma result and so warrants only a small mention here. For HD 9446 both comparison methods prefer

Table 2
Log of Spectroscopic Observations

System	Instrument	Dates	Passband	$N_{\rm data}$
HD 9446	HIRES	2013 Oct 23–2019 Oct 18	300–1100 nm	51
	SOPHIE	2006 Nov 3–2009 Mar 3	387.2–694.3 nm	79
HD 43691	HIRES	2004 Jan 10–2019 Sep 6	300–1100 nm	31
	SOPHIE	2006 Nov 5–2007 Feb 23	387.2–694.3 nm	14
	ELODIE	2004 Nov 24–2006 May 16	389.5–681.5 nm	22
HD 179079	HIRES	2004 Jul 11–2019 Aug 28	300–1100 nm	93

Table 3
MCMC Posteriors HD 9446

Parameter	Credible Interval	MAP	Units
MCMC			
P_b	$30.0608^{+0.0034}_{-0.0033}$	30.0607	days
$T\mathrm{conj}_b$	$2457790.96^{+0.56}_{-0.58}$	2457790.98	JD
e_b	$0.214^{+0.04}_{-0.041}$	0.22	
ω_b	$-2.09^{+0.21}_{-0.22}$	−2.08	radians
K_b	46.0 ± 2.1	46.1	m s^{-1}
P_c	189.6 ± 0.13	189.58	days
$T\mathrm{conj}_c$	2457724.1 ± 2.6	2457724.1	JD
e_c	$0.071^{+0.031}_{-0.032}$	0.067	
ω_c	$-2.29^{+5.2}_{-0.65}$	−3.0	radians
K_c	$60.8^{+1.9}_{-2.0}$	61	m s^{-1}
Other			
$\gamma_{\rm SOPHIE}$	≡44.2309	≡44.2309	m s^{-1}
$\gamma_{\rm HIRES}$	≡1.4458	≡1.4458	m s^{-1}
$\dot{\gamma}$	$0.0115^{+0.0025}_{-0.0023}$	0.0116	m s^{-1} day^{-1}
$\ddot{\gamma}$	≡0.0	≡0.0	m s^{-1} day^{-2}
$\sigma_{\rm SOPHIE}$	$-15.8^{+1.5}_{-1.7}$	−15.0	m s^{-1}
$\sigma_{\rm HIRES}$	$11.4^{+1.4}_{-1.2}$	10.5	m s^{-1}
Derived			
$M_b \sin i$	$0.687^{+0.056}_{-0.055}$	0.709	$M_{\rm J}$
a_b	$0.1892^{+0.0061}_{-0.0065}$	0.1844	au
$M_c \sin i$	1.71 ± 0.13	1.66	$M_{\rm J}$
a_c	$0.646^{+0.021}_{-0.022}$	0.629	au

Note. Negative jitter values in the RadVel results are equal to the positive equivalent. Reference epoch for γ, $\dot{\gamma}$, $\ddot{\gamma}$: 2457752.165903.

Table 4
MCMC Posteriors HD 179079

Parameter	Credible Interval	MAP	Units
MCMC			
P_b	$14.4708^{+0.01}_{-0.0035}$	14.47	days
$T\mathrm{conj}_b$	$2454881.84^{+0.33}_{-0.29}$	2454881.73	JD
e_b	≡0.0	≡0.0	
ω_b	≡−0.0	≡−0.0	radians
K_b	$5.84^{+0.63}_{-0.66}$	5.95	m s^{-1}
Other			
$\gamma_{\rm HIRES_{PRE2004}}$	≡−2.2151	≡−2.2151	m s^{-1}
$\gamma_{\rm HIRES}$	≡−2.0527	≡−2.0527	m s^{-1}
$\dot{\gamma}$	$0.00048^{+0.00039}_{-0.00037}$	0.00043	m s^{-1} day^{-1}
$\ddot{\gamma}$	≡0.0	≡0.0	m s^{-1} day^{-2}
$\sigma_{\rm HIRES_{PRE2004}}$	$7.4^{+7.9}_{-3.5}$	4.6	m s^{-1}
$\sigma_{\rm HIRES}$	$4.13^{+0.35}_{-0.33}$	3.97	m s^{-1}
Derived			
a_b	$0.1214^{+0.0064}_{-0.0071}$	0.1014	au
$M_b \sin i$	0.076 ± 0.012	0.053	$M_{\rm J}$

Note. Reference epoch for γ, $\dot{\gamma}$, $\ddot{\gamma}$: 2454872.463263.

models with the trend parameter free, with the best fit including a ∼4.8σ trend (see Tables 3 and B1). As the results from our speckle imaging analysis in Section 3 indicated no evidence of a stellar companion, this significant trend likely indicates an additional planet in the HD 9446 system. Further RV observation of this system is required to determine the cause of this linear trend. Note the AIC and BIC comparisons of HD 9446 preferred different models (BIC preferred e_b as a fixed parameter). However, for the purposes of determining looking for linear trends, each comparison method preferred a model with a trend.

As well as providing updated values for each planet's period, eccentricity, and semiamplitude, RadVel also derives the values for the planet semimajor axis (a) and mass (M_p sin i). These values are shown at the bottom of Tables 3–5.

Using the posteriors for the time of conjunction from the MCMC output, we calculated the transit window for each planet to use in determining if a transit of these planets had been detected (see Section 6).

5.3. Search for Additional Planets and Injection-recovery Tests

We searched for additional planet candidates in our radial velocity data using RVSearch (L. J. Rosenthal et al. 2020, in preparation), an iterative periodogram algorithm. First we define an orbital frequency/period grid over which to search, with sampling such that the difference in frequency between adjacent grid points is $\frac{1}{2\pi\tau}$, where τ is the observational baseline. Using this grid we compute a goodness-of-fit periodogram by fitting a sinusoid with a fixed period to the data for each period in the grid. We choose to measure goodness-of-fit as the change in the Bayesian Information Criterion (BIC) at each grid point between the best-fit one-planet model with the given fixed period, and the BIC value of the zero-planet fit to the data. We then fit a power law to the noise histogram (50%–95%) of the data and accordingly extrapolate a BIC detection threshold corresponding to an empirical false-alarm probability of our choice (we choose 0.003).

If one planet is detected we perform a final fit to the one-planet model with all parameters free, including eccentricity, and record the BIC of that best-fit model. We then add a second planet to our RV model and conduct another grid search, leaving the parameters of the first planet free to converge to a more optimal solution. In this case we compute the goodness-of-fit as the difference between the BIC of the best-fit one-planet model, and the BIC of the two-planet model at each fixed period in the grid. We set a detection threshold in the manner described above and continue this iterative search until

Table 5
MCMC Posteriors HD 43691

Parameter	Credible Interval	MAP	Units
MCMC			
P_b	$36.99913^{+0.00095}_{-0.00092}$	36.99932	days
$T\mathrm{conj}_b$	$2456282.91^{+0.15}_{-0.14}$	2456282.89	JD
e_b	$0.085^{+0.012}_{-0.011}$	0.087	
ω_b	-1.35 ± 0.12	-1.34	radians
K_b	130.4 ± 1.4	130.6	m s^{-1}
Other			
γ_{SOPHIE}	$\equiv -12.4134$	$\equiv -12.4134$	m s^{-1}
$\gamma_{\mathrm{HIRES_{PRE2004}}}$	$\equiv 21.0278$	$\equiv 21.0278$	m s^{-1}
γ_{HIRES}	$\equiv 21.6117$	$\equiv 21.6117$	m s^{-1}
γ_{ELODIE}	$\equiv -45.0874$	$\equiv -45.0874$	m s^{-1}
$\dot{\gamma}$	$-0.00121^{+0.00069}_{-0.00068}$	-0.00124	m s^{-1} day^{-1}
$\ddot{\gamma}$	$\equiv 0.0$	$\equiv 0.0$	m s^{-1} day^{-2}
σ_{SOPHIE}	$10.7^{+3.3}_{-2.3}$	9.8	m s^{-1}
$\sigma_{\mathrm{HIRES_{PRE2004}}}$	$-3.2^{+16.0}_{-9.6}$	-6	m s^{-1}
σ_{HIRES}	$4.85^{+0.95}_{-0.74}$	4.16	m s^{-1}
σ_{ELODIE}	-3^{+16}_{-10}	-11	m s^{-1}
Derived			
a_b	$0.238^{+0.014}_{-0.016}$	0.227	au
$M_b \sin i$	$2.57^{+0.31}_{-0.34}$	2	M_J

Note. Negative jitter values in the RadVel results are equal to the positive equivalent. Reference epoch for γ, $\dot{\gamma}$, $\ddot{\gamma}$: 2456284.051544.

the n+1th search rules out additional signals. Once we have a complete orbital model we can characterize the completeness of our search using injection-recovery tests, wherein we inject synthetic planet signals into the data and check whether RVSearch can recover that synthetic signal.

RVSearch was run on HD 9446, HD 43691, and HD 179079, and it successfully recovered each of the known planets in these systems. No additional planets were found via the search. Injection-recovery tests were then completed for each system to determine the completeness of the search, the results of which can be seen in Figure 7. Figure 7 shows the detection results of the injection-recovery tests for HD 9446 (top), HD 43691 (middle), and HD 179079 (bottom). The black dots indicate the known planets for each system whereas the smaller dots represent the injected planets. Dots that are purple are injected planets that were successfully recovered, and dots that are red are planets that were not recovered. The contouring shows the parameter spaces in which planets are likely to be recovered in light pink and those that have a low probability of detection in dark red. HD 9446 b and c and HD 43691 b are each in a parameter space with a high probability of recovery whereas HD 179079 b borders the area of low probability.

Following the methods outlined in Brandt et al. (2019) and Kiefer et al. (2019) we then attempted to constrain the mass and period of the additional companion in the HD 9446 system by calculating the difference between the Gaia (Gaia Collaboration et al. 2018) and Hipparcos (van Leeuwen 2007) positions for HD 9446, deriving the proper motion and comparing the value with the Gaia proper motion. We found no evidence from the Hipparcos to Gaia positional difference to indicate there is an acceleration. The derived proper motion from the difference between the Hipparcos and Gaia positions is consistent to the

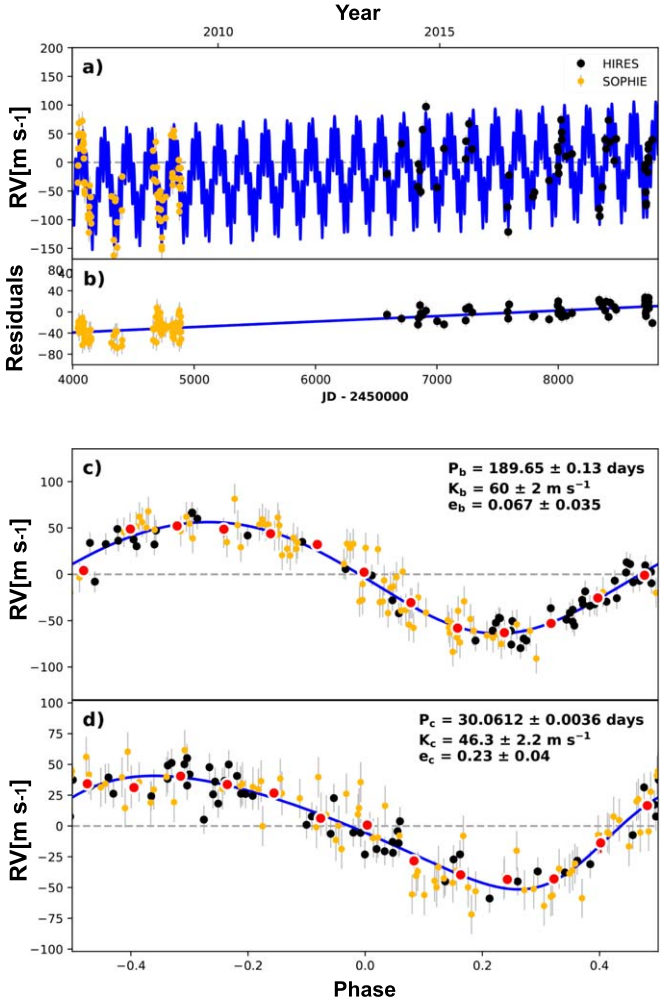

Figure 4. Best-fit two-planet Keplerian orbital model for HD 9446. The maximum likelihood model is plotted while the orbital parameters listed in Table 3 are the median values of the posterior distributions. The thin blue line is the best-fit two-planet model. We add in quadrature the RV jitter terms listed in Table 3 with the measurement uncertainties for all RVs. (b) Residuals to the best-fit two-planet model. (c) and (d) RVs phase-folded to the ephemeris of planets b and c respectively. The small point colors and symbols are the same as in panel (a). Red circles are the same velocities binned in 0.08 units of orbital phase. The phase-folded model for planets b and c are shown as the blue lines.

Gaia proper motion to within 1σ, and so we did not attempt further to constrain the period and mass of the additional companion.

6. Photometry Analysis

6.1. Data Acquisition: KELT Photometry

The KELT survey uses two robotic, wide-field telescopes to photometrically survey stars in the magnitude range $8 < V < 11$ for transiting planets (Pepper et al. 2007, 2012). It observes a set of predefined fields of size 26° × 26°, about once every 20 minutes, as long as the fields are visible. KELT uses a nonstandard passband, which is similar to a broad R-band. Details of the exoplanet discoveries and additional science results from the KELT survey are described in Pepper et al. (2018).

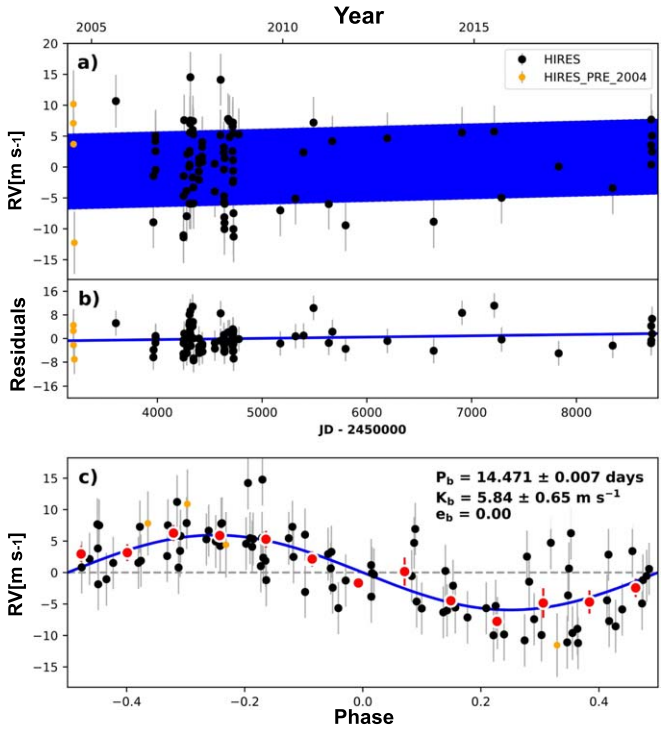

Figure 5. Best-fit one-planet Keplerian orbital model for HD 179079. The maximum likelihood model is plotted while the orbital parameters listed in Table 4 are the median values of the posterior distributions. The thin blue line is the best-fit one-planet model. We add in quadrature the RV jitter terms listed in Table 4 with the measurement uncertainties for all RVs. (b) Residuals to the best-fit one-planet model. (c) RVs phase-folded to the ephemeris of planet b. The small point colors and symbols are the same as in panel (a). Red circles are the same velocities binned in 0.08 units of orbital phase. The phase-folded model for planet b is shown as the blue line.

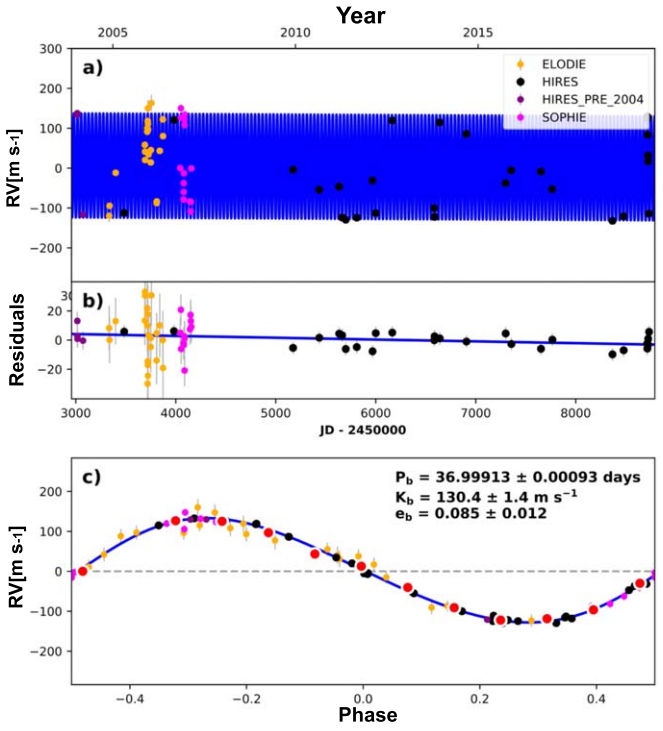

Figure 6. Best-fit one-planet Keplerian orbital model for HD 43691. The maximum likelihood model is plotted while the orbital parameters listed in Table 5 are the median values of the posterior distributions. The thin blue line is the best-fit one-planet model. We add in quadrature the RV jitter terms listed in Table 5 with the measurement uncertainties for all RVs. (b) Residuals to the best-fit one-planet model. (c) RVs phase-folded to the ephemeris of planet b. The small point colors and symbols are the same as in panel (a). Red circles are the same velocities binned in 0.08 units of orbital phase. The phase-folded model for planet b is shown as the blue line.

KELT observed HD 9446 in survey field KN02 8467 times from 2006 October 26 through 2014 December 27. The light curve has an rms scatter of 4.7 mmag. It observed HD 43691 in survey field KN04 9560 times from 2006 October 27 through 2014 December 30, with an rms scatter of 8.4 mmag. It observed HD 179079 in both survey fields KS13 and KS14. KELT observed HD 179079 in field KS13 5835 times from 2010 March 20 through 2017 September 23, with an rms scatter of 6.3 mmag, and in field KS14 3276 times from 2010 April 12 to 2014 October 23, with an rms scatter of 7.2 mmag. These observational details are provided in Table 6.

Table 6
Log of Photometric Observations

System	Instrument	Dates	Passband	N_{data}
HD 9446	APT	2015 Sep 27–2018 Feb 12	$b+y$	318
	KELT	2006 Oct 26–2014 Dec 27	R_{KELT}	8467
HD 43691	APT	2015 Sep 27–2018 Mar 15	$b+y$	412
	KELT	2006 Oct 27–2014 Dec 30	R_{KELT}	9560
HD 179079	APT	2007 Jun 6–2018 Jun 22	$b+y$	703
	KELT	2010 Mar 20–2017 Sep 23	R_{KELT}	9111

6.2. Data Acquisition: APT Photometry

We observed HD 9446, HD 43691, and HD 179079 throughout multiple observing seasons with the T10 and T12 0.80 m APTs at Fairborn Observatory in the Patagonia Mountains of southern Arizona. These APTs are two of several automated photometric, spectroscopic, and imaging telescopes operated by Tennessee State University at Fairborn. Both T10 and T12 are equipped with a two-channel precision photometer that uses a dichroic filter and two EMI 9124QB bi-alkali photomultiplier tubes to separate and simultaneously measure the Strömgren b and y passbands. The APTs are programmed to make differential brightness measurements of the program stars with respect to three comparison stars in the same field. From the raw counts, the differential magnitudes are computed as the difference in brightness between the program star and the mean brightness of the two best comparison stars. The differential magnitudes are corrected for atmospheric extinction and transformed to the Strömgren system. To improve the photometric precision, the differential b and y observations are combined into a single $(b+y)/2$ passband. Further details of the automatic telescopes, precision photometers, and observing and data reduction procedures can be found in Henry (1999) and Eaton et al. (2003). Note that the T10 and T12 APTs are functionally identical to the T8 0.80-m APT described in Henry (1999). More details on the analysis of the photometric observations for the TERMS project can be found in Henry et al. (2013).

With the T10 APT, we obtained 318 observations of HD 9446 between 2015 September 27 and 2018 February 12 and 412 observations of HD 43691 between 2015 September

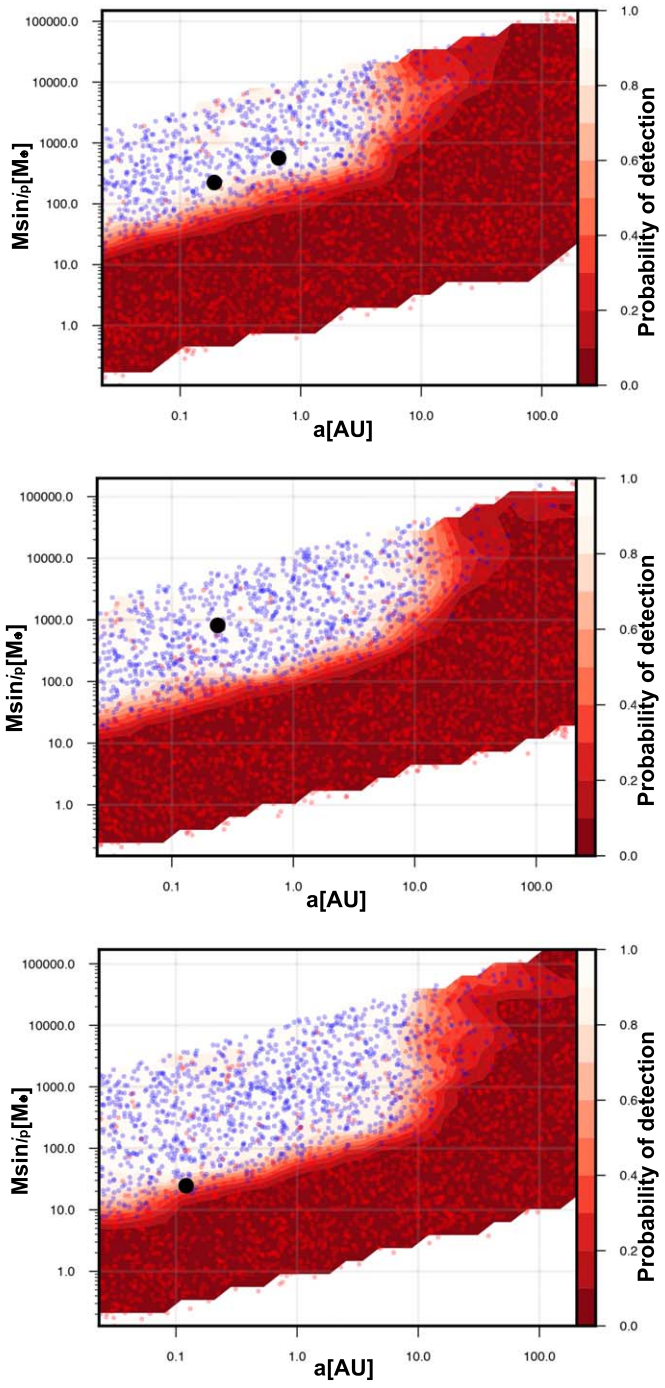

Figure 7. Injection recoveries for (top) HD 9446, (middle) HD 43691, and (bottom) HD 179079. Black dots indicate the known planets for each system, purple dots are injected planets that were successfully recovered and red dots are injected planets that were not recovered. The scale on the right of each plot shows the probability of recovery indicated by the contours on each plot. HD 9446 b and c and HD 43691 b are each in a parameter space with a high probability of recovery whereas HD 179079 b borders the area of low probability.

27 and 2018 March 15. With the T12 APT, we obtained 703 observations of HD 179079 between 2007 June 6 and 2018 June 22. The precision of the individual differential magnitudes is typically between 0.001 and 0.002 mag on good photometric nights. These observational details are provided in Table 6.

6.3. Search for Transits

Using the refined transit ephemerides and orbital periods obtained in Section 5.2 along with the photometric data from KELT and the T10 and T12 APTs, transits of the known planets were searched for in each system.

The normalized observations from all observing seasons are plotted in the top panels of Figures 8 and 9 for HD 9446 b and c, HD 179079 b, and HD 43691 b respectively.

The photometric observations within the transit window are shown for each system in the lower panels of Figures 8 and 9. The solid black line shows the transit baseline and the red line shows the binned average flux measurements for each planet. A dashed line shows the predicted transit signal expected for a central transit of the known planet. The vertical dotted lines give the $\pm 1\sigma$ uncertainty in the timing of the transit window.

A comparison of the in-transit and out-of-transit flux for each system reveals there is no significant difference in the flux received during these times. When compared to the expected transit depths calculated in Section 4 for each system, we can rule out a central transit for planet HD 9446 b to a certainty of 3.96σ. Due to gaps in the photometry data we can only rule out a transit of HD 9446 c to a certainty of 3.88σ for a planet with an impact parameter of up to $b = 0.5778$. Accounting for the data gap in the photometry of HD 43691 we can only rule out a transit to a certainty of 0.74σ for a transiting planet with an impact parameter of up to $b = 0.898$. For HD 179079 b a transit cannot be ruled out due to the combination of a relatively small planet with a large star and thus low signal-to-noise. Note that for grazing transits, limb darkening will cause a reduction in the transit depth and so these types of transits have not been ruled out in our analysis (Mandel & Agol 2002).

6.4. Photometric Variability of Host Stars

To check the photometric variability of all three host stars, we calculated and examined their Lomb–Scargle (L-S) periodograms (Lomb 1976; Scargle 1982). We calculated the L-S periodograms for each data set using astropy (Astropy Collaboration et al. 2013, 2018) for each observing season separately and also for the entire light curves, in the frequency range 0.01–1 cycles day^{-1} with 10,000 equally spaced frequency steps. Frequencies above 0.98 were excluded from the analysis due to the strong periodicity peaks caused by the diurnal observing cycle.

In each periodogram, we identified the highest periodicity peak in the unexcluded frequency range as the candidate for periodic astrophysical variability. Next, we estimated the period uncertainty from the width of the periodicity peak, which we determined by fitting the peak with a Gaussian function in the frequency range equal to the inverse of the observing baseline centered at the peak's central frequency. We also scaled the period uncertainty with the peak significance by dividing it with the square root of the normalized power of the peak (VanderPlas 2018). Then, we phase folded each light curve on the identified variability period, and determined the variability amplitude and its uncertainty by fitting the phase curve with a sine function. We also calculated the rms for each light curve before and after the sinusoidal variability fit, and false alarm probability (FAP) for each periodogram and each highest peak using the Baluev approximation (Baluev 2008).

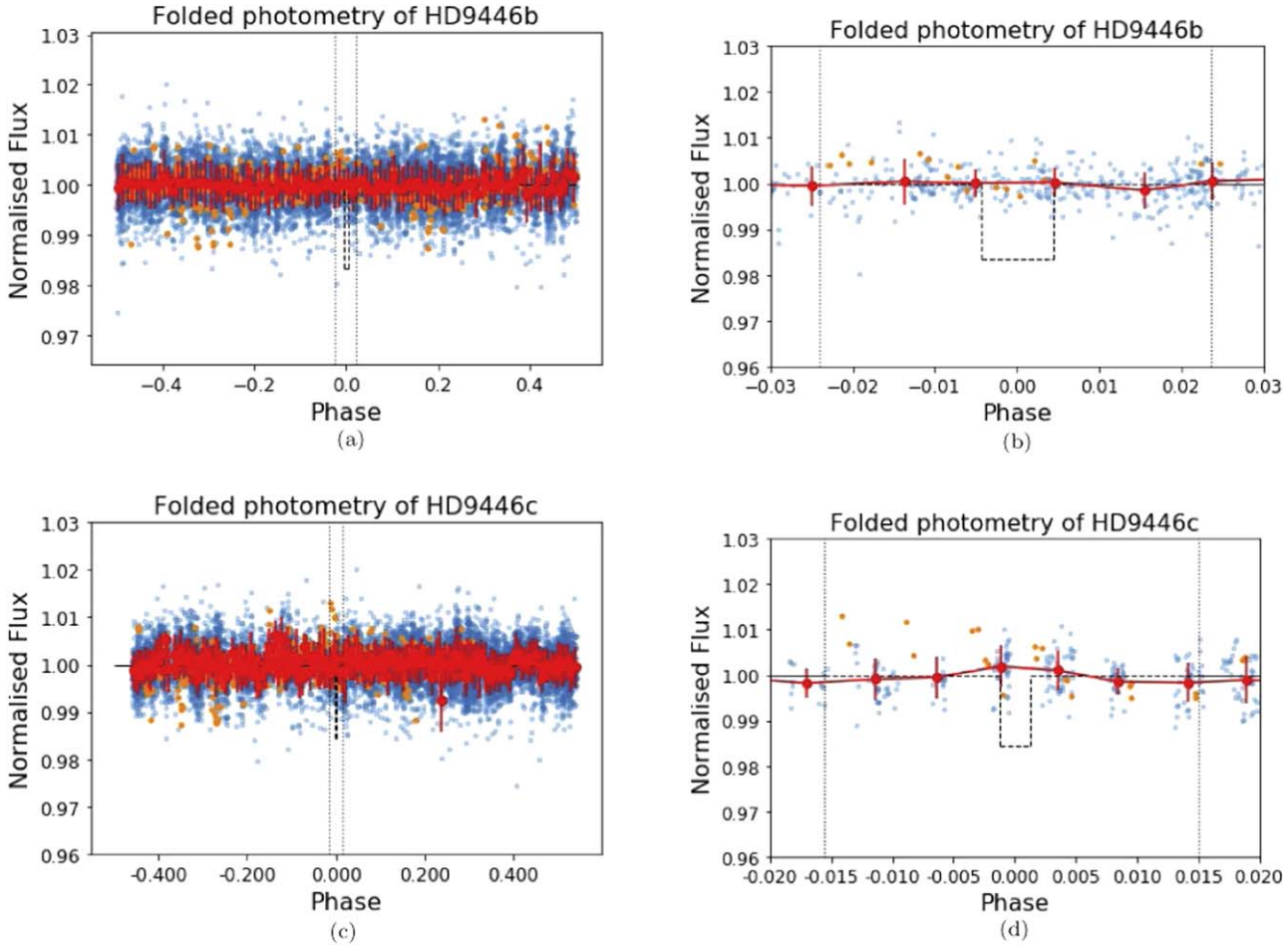

Figure 8. Top: (a) HD 9446 b phase folded KELT and APT photometry. (b) The same HD 9446 b data zoomed in on the transit window. Bottom: (c) HD 9446 c phase folded KELT and APT photometry. (d) The same HD 9446 c data zoomed in on the transit window. The transit window is defined by dotted vertical lines. The blue dots represent KELT data and orange dots represent APT data. The solid black line shows the transit baseline and the red line shows the binned average flux measurements for each planet. A dashed line shows the predicted transit signal expected for a central transit of the known planet. There is no significant difference between the normalized flux within the transit window compared to outside the transit window for either planet. For HD 9446 b this rules out a transit with a confidence of 3.96σ. Due to the data gap in the photometry of HD 9446 c we can rule out transits to a certainty of only 3.88σ for a planet with an impact parameter of up to $b = 0.5778$.

Table 7
Results of the Periodicity Analysis for HD 9446 Using the APT Data

Season	Period (days)	Full Amplitude	L-S Power	FAP	Rms Before	Rms After
2015–16	14.7 ± 2.1	0.0051 ± 0.0010	0.3026	0.0003	0.0032	0.0027
2016–17	13.8 ± 2.1	0.0037 ± 0.0008	0.2186	0.0095	0.0025	0.0022
2017–18	14.1 ± 1.4	0.0096 ± 0.0013	0.3846	<0.0001	0.0055	0.0044
all	14.39 ± 0.19	0.0063 ± 0.0007	0.2697	<0.0001	0.0043	0.0037

With the injection tests and by trial and error, we selected the following criteria for a statistically significant variability detection: (1) FAP of the periodicity peak has to be lower than 1%, (2) the full-amplitude of the variability has to be greater than the rms before variability fitting, and (3) the rms has to drop by at least 10% when removing the best-fit variability signal.

Following these criteria, we find that HD 9446 is variable with a period of 14.39 ± 0.19 days from our analysis of the whole APT light curve. We also detect the 14 day variability in every individual APT observing season (see Table 7). APT periodogram and variability phase curve of HD 9446 are shown in Figure 10. Given the small amplitude of about half a percent, the sinusoidal behavior of the variability, and the G5V spectral type of the host star, we conclude that the 14 day periodicity detected in the APT data is likely caused by starspots. This agrees with the expected stellar rotational period of $12.5^{+4.1}_{-2.5} \sin i_*$ days, which was calculated from the stellar projected rotational velocity and stellar radius, and ~10 day period, which is based on the measurement of the chromospheric activity index (Hébrard et al. 2010).

We did not detect the 14 day periodicity in the KELT data, which may be due to a number of reasons. First, the redder and broader KELT passband filter compared to the APT is dampening more variability amplitude, which typically peaks in the blue part of the spectrum (Oelkers et al. 2018). Second, the rms of most KELT observing seasons was higher than the APTs. Third, since the KELT and APT data sets do not

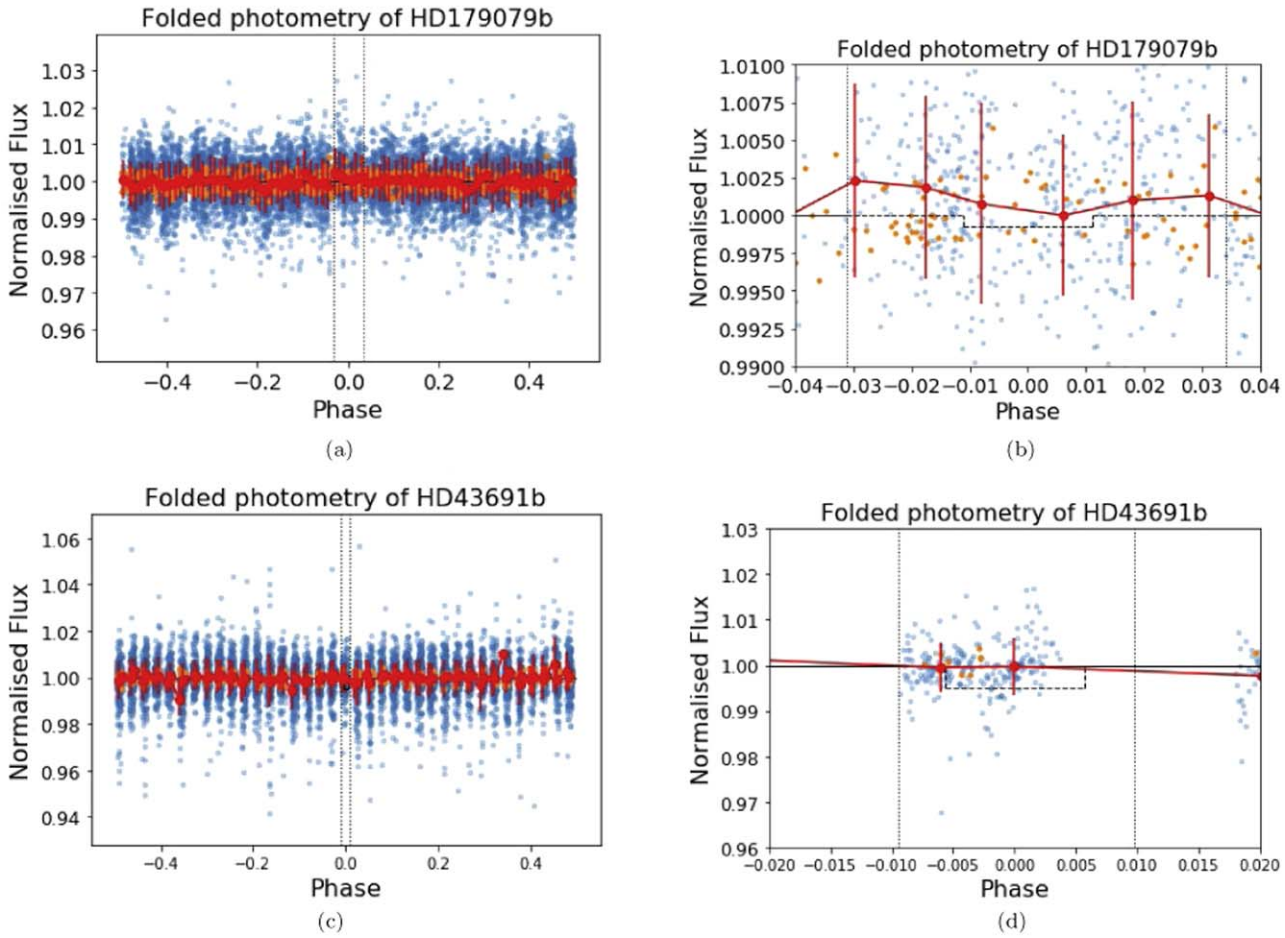

Figure 9. Top: (a) HD 179079 b phase folded KELT and APT photometry. (b) The same HD 179079 b data zoomed in on the transit window. Bottom: (c) HD 43691 b phase folded KELT and APT photometry. (d) The same HD 43691 b data zoomed in on the transit window. The transit window is defined by dotted vertical lines. The blue dots represent KELT data and orange dots represent APT data. The solid black line shows the transit baseline and the red line shows the binned average flux measurements for each planet. A dashed line shows the predicted transit signal expected for a central transit of the known planet. There is no significant difference between the normalized flux within the transit window compared to outside the transit window for either system. Due to the data gap in the photometry of HD 43691 we can rule out transits to a certainty of only 0.74σ for a planet with an impact parameter of up to $b = 0.898$. For HD 179079 b a transit cannot be ruled out due to the low signal to noise.

temporally overlap (see Table 6), the starspots may have been absent or possibly distributed differently on the stellar surface during the KELT observations. However, the KELT periodograms of all observing seasons tentatively but consistently indicate a potential presence of around 7 day periodicity, which is compatible with half of the rotational period determined with APT, and might be interpreted as a bimodal distribution of starspots on the stellar surface. However, because the variability amplitudes indicated by the KELT are significantly lower than those detected in the APT data, and do not exceed our significance criteria, they should be regarded as tentative. Instead, we set a conservative upper limit for the variability amplitude of 0.005, equal to the rms of the entire KELT light curve.

For HD 43691 and HD 179079, we did not detect any significant periodic variability in any of the APT or KELT whole or seasonal light curves. For HD 43691 we set the APT and KELT variability amplitude upper limits to 0.002 and 0.008, and for HD 179079 to 0.002 and 0.006, respectively.

Stellar chromospheric activity is tightly linked with the stellar magnetic field and is correlated with the magnetic cycle (Hall 2008) and photometric rotational modulation (Cao & Gu 2014). We do not detect any periodicities in the Ca II H and K chromospheric activity indices within the available observational timespans of HIRES observations (see Table 2) for any of the three host stars. The corresponding $\log R'_{\rm HK}$ measurements and their 1σ standard deviations for HD 9446, HD 43691, and HD 179079, are -4.71 ± 0.04, -4.85 ± 0.02, and -5.00 ± 0.01, respectively.

7. Conclusions

Using new RV data obtained from the Keck HIRES instrument we refined the orbital parameters of the known planets and looked for linear trends in the HD 9446, HD 179079, and HD 43691 systems. While our fits largely agreed with the published values for these systems, an improved solution for planet HD 9446 c was found, giving the outer planet an orbital period of 189.6 ± 0.13 days. We also found that for HD 9446 the best fit included a $\sim 4.8\sigma$ trend. As the results from our speckle imaging analysis in Section 3 indicated no evidence of a stellar companion, this likely indicates an additional planet in the HD 9446 system and so further RV monitoring of this system should be prioritized. As the discovery paper by Hébrard et al. (2010) did not report a linear trend for HD 9446, it is possible the original fit included some of

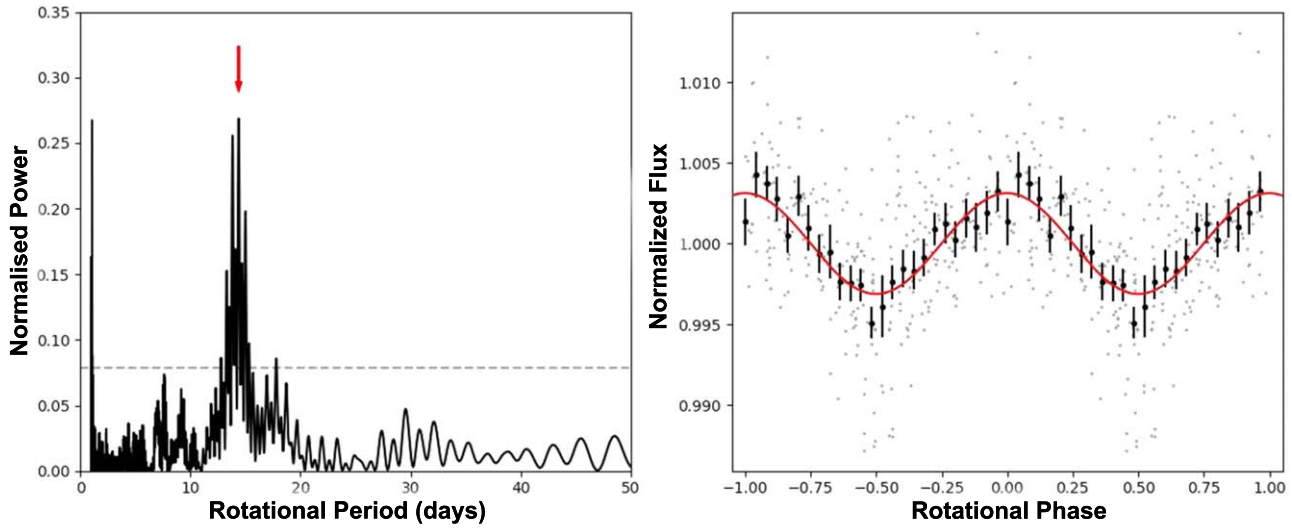

Figure 10. Detection of the periodic variability of HD 9446 using the APT light curve. Left panel: L-S periodogram. The highest periodicity peak is marked with an arrow. The peak near 1 day is caused by the diurnal cycle. The horizontal dashed line represents the FAP of 1%. Right panel: rotational phase curve. Unbinned data points are shown with small gray symbols, which have been used in the variability analysis. Larger, black symbols with error bars represent the binned phase curve with 25 bins. We only used the unbinned data in our variability analysis, and the binned data are shown here only for the purpose of visualization. The red line is the best sine fit to the unbinned rotational phase curve.

the linear trend in the orbital solution for planet c. The best fit for HD 43691 included a $\sim 1.75\sigma$ trend. While this could also indicate the presence of another unknown planet in the system, this is a low sigma result and so warrants only a small mention here.

From the refined fits for each system we produced a transit ephemeris onto which we folded precise photometry acquired with the APTs and KELT. For planet HD 9446 b a transit can be ruled out to a certainty of 3.96σ. For HD 9446 c we can rule out a transit to a certainty of 3.88σ for a planet with an impact parameter of up to $b = 0.5778$, and for planet HD 43691 a transit can be ruled out to a certainty of 0.74σ for a planet with an impact parameter of up to $b = 0.898$. Each of these stars falls into the gaps of the primary planned mission for TESS and so are unlikely to be observed by any space-based instruments. Thus these ground-based observations are essential in determining the possible transit of the planets in these systems. Given the difficulties in ruling out a transit for HD 179079 b through ground-based photometry, the total effective success probability of the experiment is significantly lower than the transit probability described in Section 4. Excluding HD 179079 b, the maximum success probability of the remaining planets is 6% assuming HD 9446 b and HD 9446 c are coplanar, 5.3% if not.

Our analysis of the T10 APT light curve revealed a 14.39 ± 0.19 days variability period of host star HD 9446. We identify this as the rotational period of the host star. Host stars HD 43691 and HD 179079 showed no evidence of significant periodic variability.

The TERMS project aids in the detection of planetary transits by refining the orbital parameters of known RV planets and calculating a revised transit ephemeris for the planet, and now combined with TESS photometry the expected yield of this collaboration is expected to be significant (Dalba et al. 2019). Already there have been detections by TESS of known planets that utilized the ongoing RV observations made by the TERMS team (Mocnik et al. 2020; J. Pepper et al. 2020, in preparation). Precision photometry from the TESS mission will be combined with the improved orbital ephemerides from TERMS observations to search for additional transiting planets in observed systems, such as the case of Pi Mensae c (Huang et al. 2018). It is expected that many more systems observed by TERMS will have as-yet undetected additional planets that will be revealed through transits and trends seen in additional RV observations, such as that found in Wang et al. (2012). TERMS observations also contribute to the stellar characterization of exoplanet host stars (Dragomir et al. 2012).

The high quality transit ephemerides are essential for follow-up observations that will occur with future space missions. For example, transmission spectroscopic observations with the James Webb Space Telescope and direct imaging with missions such as WFIRST require that both the orbit of the planets within each system and the properties of the host star be determined to a high degree of certainty (Beichman et al. 2014; Kane et al. 2018). The refined orbital properties and transit ephemerides presented in this work will be used for observing strategy development of these systems for many years, and the ruling out of transits will allow for prioritization of other targets in future transit missions, saving valuable telescope time. The targets studied by the TERMS project provide critical refinement of the orbital parameters of known planets and enable further observations to detect the existence of additional planets in orbit about each system observed.

Thanks to the anonymous referee, whose comments greatly improved the quality of the paper. G.W.H. acknowledges long-term support from NASA, NSF, Tennessee State University, and the State of Tennessee through its Centers of Excellence program. The research shown here acknowledges use of the Hypatia Catalog Database, an online compilation of stellar abundance data as described in Hinkel et al. (2014), which was supported by NASA's Nexus for Exoplanet System Science (NExSS) research coordination network and the Vanderbilt Initiative in Data-Intensive Astrophysics (VIDA). This research has made use of the NASA Exoplanet Archive, which is operated by the California Institute of

Technology, under contract with the National Aeronautics and Space Administration under the Exoplanet Exploration Program. This research has made use of NASA's Astrophysics Data System. This research has made use of the VizieR catalog access tool, CDS, Strasbourg, France (doi:10.26093/cds/vizier). The original description of the VizieR service was published in A&AS 143, 23.

Appendix A
Radial Velocity Data

Here we provide the as yet unpublished radial velocity measurements used in the analysis of this paper. Tables A1, A2, and A3 include the Keck HIRES radial velocity measurements of HD 43691, HD 9446, and HD 179079, respectively.

Table A1
Radial Velocities HD 43691[a]

Time (BJD_TDB)	RV (m s^{-1})	RV Unc. (m s^{-1})	Inst.
2453015.00100	158.82	2.15	$HIRES_{PRE2004}$
2453015.99600	154.69	2.06	$HIRES_{PRE2004}$
2453017.00100	155.06	2.05	$HIRES_{PRE2004}$
2453071.81700	−95.94	2.42	$HIRES_{PRE\ 2004}$
2453483.74700	−90.71	1.64	HIRES
2453982.12600	142.31	1.35	HIRES
2455172.97600	17.66	1.52	HIRES
2455435.12900	−32.43	1.20	HIRES
2455633.76700	−24.75	1.54	HIRES
2455663.72500	−102.27	1.56	HIRES
2455699.73300	−107.72	1.62	HIRES
2455810.13200	−102.60	1.34	HIRES
2455967.87200	−9.54	1.52	HIRES
2455999.76400	−91.19	1.65	HIRES
2456165.12600	140.90	1.43	HIRES
2456585.15400	−78.78	1.24	HIRES
2456588.06400	−100.76	1.18	HIRES
2456639.91200	136.12	1.61	HIRES
2456907.15100	107.44	1.26	HIRES
2457299.09500	−16.06	1.51	HIRES
2457356.16900	15.93	1.49	HIRES
2457652.14700	12.98	1.48	HIRES
2457765.93800	−31.24	1.36	HIRES
2458367.10100	−110.55	1.30	HIRES
2458479.08400	−99.33	1.48	HIRES
2458714.13600	151.17	1.45	HIRES
2458716.12900	145.80	1.34	HIRES
2458720.13800	104.91	1.37	HIRES
2458723.13800	53.19	1.38	HIRES
2458724.13400	38.51	1.25	HIRES
2458733.12100	−92.44	1.27	HIRES

Note.
[a] In addition, this study used the RV data from SOPHIE and ELODIE published in da Silva et al. (2007).

Table A2
Radial Velocities HD 9446[a]

Time (BJD_TDB)	RV (m s^{-1})	RV Unc. (m s^{-1})	Inst.
2456588.95400	−19.84	1.44	HIRES
2456708.72400	33.14	1.59	HIRES
2456844.12600	−42.03	1.24	HIRES
2456849.12800	−2.48	1.57	HIRES
2456861.05200	−13.62	1.66	HIRES
2456867.09011	−50.61	0.90	HIRES
2456882.11200	57.61	1.55	HIRES
2456910.11000	97.61	1.72	HIRES
2457001.76600	−43.22	1.47	HIRES
2457058.71700	24.48	1.59	HIRES
2457237.13500	6.41	1.23	HIRES
2457240.12500	37.39	1.30	HIRES
2457265.11900	67.90	1.47	HIRES
2457291.00200	23.56	1.53	HIRES
2457582.13400	−77.37	1.55	HIRES
2457587.11200	−120.59	1.45	HIRES
2457595.03900	−21.99	1.42	HIRES
2457791.73900	−59.49	1.91	HIRES
2457802.70400	−51.55	1.67	HIRES
2457925.12800	−31.16	1.77	HIRES
2457995.00500	27.36	1.64	HIRES
2457999.97500	19.30	1.71	HIRES
2458000.97500	−6.74	1.54	HIRES
2458003.00600	−19.13	1.71	HIRES
2458023.94400	74.72	1.69	HIRES
2458028.90700	52.95	1.79	HIRES
2458029.87500	39.92	1.83	HIRES
2458065.81000	11.05	1.88	HIRES
2458112.69300	15.22	1.64	HIRES
2458337.12000	−80.41	1.72	HIRES
2458341.10700	−93.33	1.58	HIRES
2458364.03100	−42.91	1.61	HIRES
2458385.99900	40.13	1.56	HIRES
2458394.03500	24.10	1.75	HIRES
2458414.89600	74.24	1.63	HIRES
2458426.97000	36.00	1.81	HIRES
2458462.74500	3.38	1.64	HIRES
2458476.78700	41.47	1.78	HIRES
2458714.03700	−11.36	1.24	HIRES
2458715.05300	−5.62	1.43	HIRES
2458716.04400	−3.44	1.22	HIRES
2458720.03800	−51.58	1.28	HIRES
2458723.03000	−74.25	1.27	HIRES
2458724.04400	−71.00	1.29	HIRES
2458737.88700	−16.74	1.91	HIRES
2458739.02800	0.23	1.69	HIRES
2458739.93500	8.59	1.69	HIRES
2458742.98100	23.66	1.69	HIRES
2458743.97100	31.39	1.64	HIRES
2458746.97100	7.93	1.64	HIRES
2458774.89000	40.19	1.77	HIRES

Note.
[a] In addition, this study used the RV data from SOPHIE published in Hébrard et al. (2010).

Table A3
Radial Velocities HD 179079

Time (BJD_TDB)	RV (m s^{-1})	RV Unc. (m s^{-1})	Inst.
2453197.997	5.02	2.21	HIRES
2453198.963	8.11	2.96	HIRES
2453199.909	1.63	2.45	HIRES
2453208.025	−14.32	2.1	HIRES
2453603.86	8.87	1.57	HIRES
2453961.876	−10.82	1.39	HIRES
2453963.867	−3.23	1.41	HIRES
2453981.76	2.18	1.38	HIRES
2453982.806	3.3	1.43	HIRES
2453983.77	0.82	1.34	HIRES
2453984.845	−2.38	1.27	HIRES
2454249.037	−13.09	1.28	HIRES
2454250.08	−13.21	1.33	HIRES
2454251.057	−6.49	1.08	HIRES
2454251.936	−3.46	1	HIRES
2454256.09	5.71	1.12	HIRES
2454279.039	−5.75	1.07	HIRES
2454280.047	−9.91	1.16	HIRES
2454286.038	0.26	1.36	HIRES
2454304.972	−2.15	1.19	HIRES
2454305.972	−8.05	1.17	HIRES
2454306.972	0.12	1.16	HIRES
2454308.001	−1.76	1.24	HIRES
2454308.969	0.43	1.18	HIRES
2454309.965	−1.7	1.2	HIRES
2454310.957	5.17	1.15	HIRES
2454311.955	5.03	1.21	HIRES
2454312.95	3.42	1.28	HIRES
2454313.948	5.51	1.16	HIRES
2454314.957	12.62	1.07	HIRES
2454318.863	−7.87	1.15	HIRES
2454335.965	−3.47	1.23	HIRES
2454336.989	4.31	1.32	HIRES
2454339.853	5.58	1.1	HIRES
2454343.888	3.48	1.18	HIRES
2454344.944	−5.03	1.21	HIRES
2454345.759	−7.69	1.18	HIRES
2454396.73	−2.48	1.24	HIRES
2454397.757	−3.77	1.13	HIRES
2454398.742	−0.45	1.12	HIRES
2454399.725	−1.18	1.35	HIRES
2454427.745	−0.23	1.19	HIRES
2454428.704	1.42	1.19	HIRES
2454429.686	2.22	1.18	HIRES
2454430.683	−1.02	1.23	HIRES
2454548.152	−1.25	1.23	HIRES
2454549.145	−5.61	1.26	HIRES

Table A3
(Continued)

Time (BJD_TDB)	RV (m s^{-1})	RV Unc. (m s^{-1})	Inst.
2454602.977	3.27	1.17	HIRES
2454603.997	12.27	1.43	HIRES
2454634.049	0.33	1.36	HIRES
2454634.978	1.22	1.25	HIRES
2454636.021	−2.47	1.21	HIRES
2454637.067	−6.63	1.26	HIRES
2454638.014	−7.45	1.2	HIRES
2454639.045	−9.97	1.23	HIRES
2454640.127	−11.82	1.35	HIRES
2454641.006	−10.92	1.19	HIRES
2454642.104	−7.72	1.28	HIRES
2454644.1	−0.49	1.23	HIRES
2454674.838	5.57	1.16	HIRES
2454688.849	5.49	1.25	HIRES
2454690.022	3.18	1.34	HIRES
2454717.772	0.94	1.16	HIRES
2454718.791	4.69	1.13	HIRES
2454719.803	3.68	1.15	HIRES
2454720.842	5.43	1.18	HIRES
2454721.829	−4.16	1.16	HIRES
2454722.772	−0.6	1.19	HIRES
2454723.765	−2.57	1.23	HIRES
2454724.779	−3.78	1.22	HIRES
2454725.77	−11.84	1.29	HIRES
2454726.766	−9.1	1.1	HIRES
2454727.843	−12.92	1.21	HIRES
2454777.763	3.5	1.33	HIRES
2455173.69	−8.87	1.33	HIRES
2455319.076	−7.09	1.29	HIRES
2455395.94	0.52	1.26	HIRES
2455490.74	5.34	1.25	HIRES
2455636.122	−7.95	1.13	HIRES
2455671.065	2.65	1.17	HIRES
2455796.777	−11.46	1.3	HIRES
2456195.751	2.78	1.25	HIRES
2456637.686	−10.66	1.6	HIRES
2456908.727	3.82	1.11	HIRES
2457215.937	3.98	1.38	HIRES
2457285.742	−6.67	1.26	HIRES
2457831.152	−1.65	1.21	HIRES
2458346.797	−5.47	1.45	HIRES
2458713.775	1.47	1.26	HIRES
2458714.745	5.62	1.24	HIRES
2458715.741	−1.67	1.26	HIRES
2458722.768	3.01	1.16	HIRES
2458723.741	0.43	1.22	HIRES

Appendix B
RadVel Model Comparison Tables

In this section we present the model comparison summary with both Akaike information criterion (AIC) and Bayesian Information criterion (BIC) values for HD 9446, HD 43691, and HD 179079, respectively.

Table B1
Model Comparison HD 9446

AICc Qualitative Comparison	Free Parameters	$N_{\rm free}$	$N_{\rm data}$	Rms	$\ln \mathcal{L}$	BIC	AICc	ΔAICc
AICc Favored Model	e_b, K_b, e_c, K_c, $\dot{\gamma}$, σ, γ	13	129	14.16	−522.62	1098.67	1064.66	0.00
Nearly Indistinguishable	K_b, e_c, K_c, $\dot{\gamma}$, σ, γ	11	129	14.50	−526.08	1095.24	1066.04	1.38
Ruled Out	K_b, e_c, K_c, σ, γ	10	129	15.54	−536.56	1110.87	1084.14	19.48
	e_b, K_b, e_c, K_c, σ, γ	12	129	15.29	−534.51	1117.00	1085.37	20.71
	e_b, K_b, K_c, $\dot{\gamma}$, σ, γ	11	129	15.79	−536.49	1115.84	1086.64	21.98
	K_b, K_c, $\dot{\gamma}$, σ, γ	9	129	16.26	−540.43	1113.33	1089.11	24.45
	e_b, K_b, K_c, σ, γ	10	129	16.44	−543.58	1124.53	1097.79	33.13
	K_b, K_c, σ, γ	8	129	16.88	−546.73	1120.75	1099.07	34.41
	K_b, $\dot{\gamma}$, σ, γ	6	129	33.75	−636.54	1292.58	1276.11	211.45
	e_b, K_b, $\dot{\gamma}$, σ, γ	8	129	33.32	−635.00	1298.24	1276.57	211.91
	K_b, σ, γ	5	129	34.06	−638.04	1290.49	1276.68	212.02
	e_b, K_b, σ, γ	7	129	33.74	−637.10	1297.53	1278.44	213.78
	K_c, $\dot{\gamma}$, σ, γ	6	129	43.66	−668.97	1357.00	1340.53	275.87
	K_c, σ, γ	5	129	44.08	−670.22	1354.68	1340.87	276.21
	e_c, K_c, σ, γ	7	129	43.87	−669.74	1363.49	1344.40	279.74
	e_c, K_c, $\dot{\gamma}$, σ, γ	8	129	43.53	−668.69	1366.22	1344.54	279.88
	σ, γ	2	129	53.53	−694.73	1389.28	1383.66	319.00
	$\dot{\gamma}$, σ, γ	3	129	53.20	−694.03	1392.73	1384.35	319.69
	e_b, K_b, e_c, K_c, $\dot{\gamma}$, γ	11	129	14.59	−1720.01	3483.12	3453.92	2389.26
	K_b, e_c, K_c, $\dot{\gamma}$, γ	9	129	15.07	−1806.56	3646.11	3621.89	2557.23
	e_b, K_b, K_c, $\dot{\gamma}$, γ	9	129	16.26	−2016.26	4064.95	4040.73	2976.07
	K_b, K_c, $\dot{\gamma}$, γ	7	129	16.76	−2101.19	4224.76	4205.66	3141.00
	e_b, K_b, e_c, K_c, γ	10	129	16.11	−2141.88	4318.99	4292.26	3227.60
	K_b, e_c, K_c, γ	8	129	16.18	−2179.70	4384.89	4363.21	3298.55
	e_b, K_b, K_c, γ	8	129	17.38	−2352.36	4729.83	4708.15	3643.49
	K_b, K_c, γ	6	129	17.65	−2412.14	4839.35	4822.88	3758.22
	e_b, K_b, $\dot{\gamma}$, γ	6	129	34.00	−11728.06	23472.15	23455.67	22391.01
	K_b, $\dot{\gamma}$, γ	4	129	33.74	−12298.96	24604.46	24593.34	23528.68
	e_b, K_b, γ	5	129	35.59	−12696.38	25397.32	25383.51	24318.85
	K_b, γ	3	129	35.02	−13079.73	26156.88	26148.49	25083.83
	e_c, K_c, $\dot{\gamma}$, γ	6	129	44.71	−17516.10	35051.55	35035.08	33970.42
	K_c, $\dot{\gamma}$, γ	4	129	44.42	−17565.82	35141.27	35130.16	34065.50
	e_c, K_c, γ	5	129	45.43	−18105.53	36225.48	36211.66	35147.00
	K_c, γ	3	129	45.07	−18160.39	36325.53	36317.14	35252.48
	$\dot{\gamma}$, γ	1	129	53.39	−27445.77	54886.50	54883.67	53819.01
	γ	0	129	53.60	−27570.93	55131.95	55131.95	54067.29

Table B2
Model Comparison HD 43691

AICc Qualitative Comparison	Free Parameters	$N_{\rm free}$	$N_{\rm data}$	Rms	$\ln \mathcal{L}$	BIC	AICc	ΔAICc
AICc Favored Model	e_b, K_b, $\dot{\gamma}$, σ, γ	10	67	11.47	−224.05	501.61	483.49	0.00
Nearly Indistinguishable	e_b, K_b, σ, γ	9	67	11.48	−226.02	501.65	484.96	1.47
Ruled Out	K_b, σ, γ	7	67	13.41	−245.37	531.91	518.38	34.89
	K_b, $\dot{\gamma}$, σ, γ	8	67	13.37	−244.83	535.08	519.92	36.43
	σ, γ	4	67	89.30	−373.15	774.61	766.44	282.95
	$\dot{\gamma}$, σ, γ	5	67	88.39	−372.45	777.42	767.38	283.89

Table B3
Model Comparison HD 179079

AICc Qualitative Comparison	Free Parameters	N_{free}	N_{data}	Rms	$\ln \mathcal{L}$	BIC	AICc	ΔAICc
AICc Favored Model	K_b, σ, γ	5	93	4.19	−268.46	549.03	537.06	0.00
Nearly Indistinguishable	K_b, $\dot{\gamma}$, σ, γ	6	93	4.16	−267.75	552.14	537.93	0.87
Ruled Out	σ, γ	2	93	6.06	−301.06	600.65	595.72	58.66
	$\dot{\gamma}$, σ, γ	3	93	6.05	−300.95	604.96	597.63	60.57

ORCID iDs

Michelle L. Hill https://orcid.org/0000-0002-0139-4756
Stephen R. Kane https://orcid.org/0000-0002-7084-0529
Gregory W. Henry https://orcid.org/0000-0003-4155-8513
Joshua Pepper https://orcid.org/0000-0002-3827-8417
Natalie R. Hinkel https://orcid.org/0000-0003-0595-5132
Paul A. Dalba https://orcid.org/0000-0002-4297-5506
Benjamin J. Fulton https://orcid.org/0000-0003-3504-5316
Keivan G. Stassun https://orcid.org/0000-0002-3481-9052
Lee J. Rosenthal https://orcid.org/0000-0001-8391-5182
Andrew W. Howard https://orcid.org/0000-0001-8638-0320
Steve B. Howell https://orcid.org/0000-0002-2532-2853
Mark E. Everett https://orcid.org/0000-0002-0885-7215
Tabetha S. Boyajian https://orcid.org/0000-0001-9879-9313
Debra A. Fischer https://orcid.org/0000-0003-2221-0861
Joseph E. Rodriguez https://orcid.org/0000-0001-8812-0565
Thomas G. Beatty https://orcid.org/0000-0002-9539-4203
David J. James https://orcid.org/0000-0001-5160-4486

References

Akeson, R. L., Chen, X., Ciardi, D., et al. 2013, PASP, 125, 989
Astropy Collaboration, Price-Whelan, A. M., Sipőcz, B. M., et al. 2018, AJ, 156, 123
Astropy Collaboration, Robitaille, T. P., Tollerud, E. J., et al. 2013, A&A, 558, A33
Baluev, R. V. 2008, MNRAS, 385, 1279
Baranne, A., Queloz, D., Mayor, M., et al. 1996, A&AS, 119, 373
Baumann, P., Ramírez, I., Meléndez, J., Asplund, M., & Lind, K. 2010, A&A, 519, A87
Beatty, T. G., & Gaudi, B. S. 2008, ApJ, 686, 1302
Beichman, C., Benneke, B., Knutson, H., et al. 2014, PASP, 126, 1134
Brandt, T. D., Dupuy, T. J., & Bowler, B. P. 2019, AJ, 158, 140
Brewer, J. M., Fischer, D. A., Valenti, J. A., & Piskunov, N. 2016, ApJS, 225, 32
Brewer, J. M., Giguere, M., & Fischer, D. A. 2014, PASP, 126, 48
Brugamyer, E., Dodson-Robinson, S. E., Cochran, W. D., & Sneden, C. 2011, ApJ, 738, 97
Cao, D.-t., & Gu, S.-h. 2014, AJ, 147, 38
Charbonneau, D., Brown, T. M., Latham, D. W., & Mayor, M. 2000, ApJL, 529, L45
Chen, J., & Kipping, D. 2016, ApJ, 834, 17
da Silva, R., Udry, S., Bouchy, F., et al. 2007, A&A, 473, 323
Dalba, P. A., Kane, S. R., Barclay, T., et al. 2019, PASP, 131, 034401
Dragomir, D., Kane, S. R., Henry, G. W., et al. 2012, ApJ, 754, 37
Eaton, J. A., Henry, G. W., & Fekel, F. C. 2003, ASSL, 288, 189
Fulton, B. J., Petigura, E. A., Blunt, S., & Sinukoff, E. 2018, PASP, 130, 044504
Gaia Collaboration, Brown, A. G. A., Vallenari, A., et al. 2018, A&A, 616, A1
Gonzalez, G., Carlson, M. K., & Tobin, R. W. 2010a, MNRAS, 403, 1368
Gonzalez, G., Carlson, M. K., & Tobin, R. W. 2010b, MNRAS, 407, 314
Hall, J. C. 2008, LRSP, 5, 2
Hébrard, G., Bonfils, X., Ségransan, D., et al. 2010, A&A, 513, A69
Henry, G. W. 1999, PASP, 111, 845
Henry, G. W., Kane, S. R., Wang, S. X., et al. 2013, ApJ, 768, 155
Henry, G. W., Marcy, G. W., Butler, R. P., & Vogt, S. S. 2000, ApJL, 529, L41
Hinkel, N. R., Timmes, F. X., Young, P. A., Pagano, M. D., & Turnbull, M. C. 2014, AJ, 148, 54
Ho, S., & Turner, E. L. 2011, ApJ, 739, 26
Horch, E. P., Veillette, D. R., Baena Gallé, R., et al. 2009, AJ, 137, 5057
Howell, S. B., Everett, M. E., Sherry, W., Horch, E., & Ciardi, D. R. 2011, AJ, 142, 19
Huang, C. X., Burt, J., Vanderburg, A., et al. 2018, ApJS, 235, 2
Jofré, P., Heiter, U., Soubiran, C., et al. 2015, A&A, 582, A81
Kane, S. R., Dalba, P. A., Horner, J., et al. 2019, ApJ, 875, 74
Kane, S. R., Howell, S. B., Horch, E. P., et al. 2014, ApJ, 785, 93
Kane, S. R., Mahadevan, S., von Braun, K., Laughlin, G., & Ciardi, D. R. 2009, PASP, 121, 1386
Kane, S. R., Meshkat, T., & Turnbull, M. C. 2018, AJ, 156, 267
Kane, S. R., & von Braun, K. 2008, ApJ, 689, 492
Kang, W., Lee, S.-G., & Kim, K.-M. 2011, ApJ, 736, 87
Kiefer, F., Hébrard, G., Sahlmann, J., et al. 2019, A&A, 631, A125
Kipping, D. M. 2012, MNRAS, 427, 2487
Kipping, D. M., & Sandford, E. 2016, MNRAS, 463, 1323
Kurucz, R. L. 2013, ATLAS12: Opacity Sampling Model Atmosphere Program, Astrophysics Source Code Library, ascl:1303.024
Laughlin, G., Crismani, M., & Adams, F. C. 2011, ApJL, 729, L7
Lodders, K., Palme, H., & Gail, H.-P. 2009, LanB, 4B, 712
Lomb, N. R. 1976, Ap&SS, 39, 447
Lopez, E. D., & Fortney, J. J. 2013, ApJ, 776, 2
Maldonado, J., & Villaver, E. 2016, A&A, 588, A98
Maldonado, J., Villaver, E., & Eiroa, C. 2013, A&A, 554, A84
Mandel, K., & Agol, E. 2002, ApJL, 580, L171
Ment, K., Fischer, D. A., Bakos, G., Howard, A. W., & Isaacson, H. 2018, AJ, 156, 213
Mocnik, T., Pepper, J., Kane, S., et al. 2020, AAS Meeting, 235, 349.07
Oelkers, R. J., Rodriguez, J. E., Stassun, K. G., et al. 2018, AJ, 155, 39
Paunzen, E. 2015, A&A, 580, A23
Pepper, J., Kuhn, R. B., Siverd, R., James, D., & Stassun, K. 2012, PASP, 124, 230
Pepper, J., Pogge, R. W., DePoy, D. L., et al. 2007, PASP, 119, 923
Pepper, J., Stassun, K. G., & Gaudi, B. S. 2018, in Handbook of Exoplanets, ed. H. Deeg & J. Belmonte (Cham: Springer), 128
Perruchot, S., Kohler, D., Bouchy, F., et al. 2008, Proc. SPIE, 7014, 70140J
Petigura, E. A., & Marcy, G. W. 2011, ApJ, 735, 41
Ramírez, I., Allende Prieto, C., & Lambert, D. L. 2013, ApJ, 764, 78
Ramírez, I., Fish, J. R., Lambert, D. L., & Prieto, C. A. 2012, ApJ, 756, 46
Ramírez, I., Meléndez, J., & Asplund, M. 2009, A&A, 508, L17
Ramírez, I., Meléndez, J., & Asplund, M. 2014, A&A, 561, A7
Ramírez, I., Prieto, C. A., & Lambert, D. L. 2007, A&A, 465, 271
Santos, N. C., Sousa, S. G., Mortier, A., et al. 2013, A&A, 556, A150
Scargle, J. D. 1982, ApJ, 263, 835
Schlegel, D. J., Finkbeiner, D. P., & Davis, M. 1998, ApJ, 500, 525
Seager, S., & Sasselov, D. D. 2000, ApJ, 537, 916
Stassun, K. G., Collins, K. A., & Gaudi, B. S. 2017, AJ, 153, 136
Stassun, K. G., Corsaro, E., Pepper, J. A., & Gaudi, B. S. 2018, AJ, 155, 22
Stassun, K. G., & Torres, G. 2016, AJ, 152, 180
Stassun, K. G., & Torres, G. 2018, ApJ, 862, 61
Stevens, D. J., & Gaudi, B. S. 2013, PASP, 125, 933

Tokovinin, A., Fischer, D. A., Bonati, M., et al. 2013, PASP, 125, 1336
Torres, G., Andersen, J., & Giménez, A. 2010, A&ARv, 18, 67
Valenti, J. A., Fischer, D., Marcy, G. W., et al. 2009, ApJ, 702, 989
Valenti, J. A., & Fischer, D. A. 2005, ApJS, 159, 141
Valenti, J. A., & Piskunov, N. 1996, A&AS, 118, 595
van Leeuwen, F. 2007, A&A, 474, 653
VanderPlas, J. T. 2018, ApJS, 236, 16
Vogt, S. S., Allen, S. L., Bigelow, B. C., et al. 1994, Proc. SPIE, 2198, 362
Wang, X., Wright, J. T., Cochran, W., et al. 2012, ApJ, 761, 1
Wittrock, J. M., Kane, S. R., Horch, E. P., et al. 2016, AJ, 152, 149
Wittrock, J. M., Kane, S. R., Horch, E. P., et al. 2017, AJ, 154, 184